Assessing Spacing Impact on the Wind Turbine Array Boundary Layer via Proper Orthogonal Decomposition

Naseem Ali, Nicholas Hamilton, and Raúl Bayoán Cal

Department of Mechanical and Materials Engineering,

Portland State University, Portland, OR 97207

Abstract

As wind farms become larger, the spacing between the turbines becomes a significant design element that can impose serious economic constraints. Therefore the investigation of the turbine spacing and its effect on the produced power and flow structure are crucial for future development of wind energy. A 4 $\times$ 3 array of wind turbines was assembled in a wind tunnel with four cases to study the influence based on streamwise and spanwise spacings. The four cases are chosen with a spacing of 6D and 3D in the streamwise, and 3D and 1.5D in the spanwise direction. Data are extracted experimentally using stereo particle-image velocimetry and analyzed statistically. The maximum mean velocity is displayed at the upstream of the turbine with the spacing of $6D$ and $3D$, in the streamwise and spanwise direction, respectively. Downstream the turbines confirms a notable influence of the streamwise spacing is shown when the spanwise spacing equals to $3D$. Streamwise averaging is performed after shifting the upstream windows toward the downstream flow to quantify wake statistics independent of differences in spacing. The largest and smallest averaged Reynolds stress, and flux locates at cases $3D \times 3D$ and $6D \times 1.5D$, respectively. Snapshot proper orthogonal decomposition is employed to identify the flow structures based on the turbulent kinetic energy content. The case of spacing $6D \times 1.5D$ possesses the maximum turbulent kinetic energy content in the first mode compared with other cases. Thus, the upstream flow of each of the four cases converges faster than the flow downstream of the wind turbine in terms of the represented cumulative turbulent kinetic energy. The streamwise-averaged profile of the Reynolds stress is reconstructed using a specific number of modes for each case; the case of $6D \times 1.5D$ spacing displays the fastest reconstruction. Intermediate modes are also used to reconstruct the averaged profile and show that the intermediate scales are responsible for taking the shape of the original profile. The impact of the streamwise and spanwise spacings in power produced is quantified, where the maximum power produced corresponds with the case of greatest turbine spacing.

PACS numbers:

I. INTRODUCTION

Impacts on siting wind turbines in the wind farm include interaction between wakes, decreased wind velocity and an increased in the accumulated dynamic load on the downstream turbines. Turbine wakes lead to loss an average 10-20% of the total potential power output of wind turbine array[1]. **Extensive experimental and numerical studies focus on the wake properties in terms of mean flow characteristics used to obtain estimates of power production** [2–5]. Wake growth particularly depends on the shape and magnitude of the velocity deficit that relies on the ground roughness, flow above the canopy and spacing between the turbines.

Although there are many studies dealing with the effect of the density of turbines on the wake recovery, it is still a debated question. **The actual spacing according to the Nysted farm is 10.5 diameters (D) downstream by 5.8D spanwise at the exact row (ER). The wind direction at the ER is 278° and mean wind direction can slightly offset from ER by ± 15° [6].** According to the Horns Rev farm is $7D$, actual spacing along the bulk flow direction and $9.4D$ or $10.4D$ along the diagonal. Barthelmie and Jensen [7] showed that the spacing in the Nysted farm is responsible for 68-76% of the farm efficiency variation and for wind speed below 15 ms^{-1}, the efficiency will increase 1.3% for everyone diameter increasing in spacing. Hansen et al. [8] pointed out that the variations in the power deficit for different spacing were almost negligible at approximately $10D$ into Horns Rev farm in spite of a large power deficit resulting from smaller turbine spacing. In addition, the mean power deficit is similar along single wind turbine rows when inflow direction is constant and the wind speed ranges from 6 to 10 ms^{-1}. Furthermore, the maximum deficit occurs between the first and the second row of turbines. **Calaf et al. [4] utilized large eddy simulation to simulate infinite aligned wind farms of three different spacing ratio and five different turbine occupied areas to study the turbine spacing effects on the mean velocity profiles.** González-Longatt et al. [9] found that when the downstream and spanwise spacing increased, the wake coefficient, which represents the ratio of total power output with and without wake effects, increased. They further found that the effect of the incoming flow direction on the wake coefficient increased when the spacing of the array is reduced. Meyers and Meneveau [10] studied the optimal spacing in a fully developed wind farm with considerable limitations, including neutral stratification and

flat terrain with no topography. The results highlight that depending on the ratio of land cost and turbine cost, the optimal spacing might be $15D$ instead of $7D$. Stevens [11] used the effective roughness length performed by LES to predict the wind velocity at hub height depending on the streamwise and spanwise spacing, and the turbine loading factors. Also showing that optimal spacing depends on the wind farm length in addition to the factors suggested in Meyers and Meneveau [10]. **Nilsson et al. [12] performed the large eddy simulations of the Lillgrund wind farm. They imposed pre-generated turbulence and wind shear in the computational domain to simulate realistic atmospheric conditions. The streamwise and spanwise spacing of the wind farm is 3.3D and 4.6D. In addition, a turbine located close to the center of the wind farm is not present, thus a limited spacing farm is accounted for as well as double its streamwise/spanwise lengths are also represented. Consequently, their results are highly applicable in the current study, although the foci are on turbulence intensity effects as well as yaw angle.**

Further investigation in array optimization is undertaken by changing the alignment of the wind farm often referred to as staggered wind farms. Meyers and Meneveau [13] compared aligned versus staggered wind farms; the latter yielding a 5% increase in extracted power. Yang et al. [14] used LES to study the influence of the streamwise and spanwise spacings on the power output in aligned wind farms under fully developed regime. Their result showed that when the streamwise spacing is larger the power output is higher, and the streamwise spacing shows more impact on the design of aligned wind farms than the spanwise spacing. Churchfield et al. [15, 16] applied a precursor LES of the atmospheric boundary layer to generate inflow conditions in the Lillgrund wind farm. Simulated time-averaged power production for the aligned case strongly matches the field measurements up to the sixth turbine row. Wu and Porté-Agel [17] investigated turbulent flow within and above an aligned and a staggered wind farms under neutral conditions using validated LES framework. They showed the cumulative wakes are perceived to possess strong lateral interaction in the staggered case. In contrast, the lateral interaction between cumulated wakes is vulnerable in the aligned wind farm. Archer et al. [18] quantified the influence of wind farm layout on wind power production. They verified that the Increas-

ing the turbine spacing in the predominant wind direction and staggering every second row improve wake recovery and maximize the power production. Stevens et al. [19] used LES model to investigate the power output and wake effects in aligned and staggered wind farms with different streamwise and spanwise turbine spacing. In the staggered configuration, power output in fully developed flow depends mainly on the spanwise and streamwise spacing, whereas in the aligned configuration, power strongly depends on the streamwise spacing. Recently, Hamilton et al. [20] investigated the effect of wind turbine configuration on the wake interaction and canopy layer. They considered standard Cartesian and row-offset configurations. The results showed that the maximum flux of kinetic energy increases about 7.5% in the exit row of offset configuration compared with the Cartesian arrangement.

As a result of wind farms becoming larger, the cost of the land-surface is considerable and becomes a critical factor in the overall value of the wind farm. The spacing between the turbines is an important design factor in terms of overall wind turbine performance and economic constraints. Therefore, the investigation of limited spacing is important as it affects the wind turbine-generated wakes as well as the power production. The current work compares the turbulent flow in various configurations of the array, where the streamwise and spanwise spacing are varied. The performance of the arrays is illustrated by analyzing the mean velocity, Reynolds shear stress, mean kinetic energy flux and power measurement. In addition, the proper orthogonal decomposition (POD) is employed to identify coherent structures of the turbulent wake associated with variation in spacing. The reconstruction algorithm of the POD is also applied to reconstruct the Reynolds shear stress and show the fast rebuilding based on the spacing variation.

This paper is organized as follows. In Section II the mathematical formulation for the proper orthogonal decomposition is stated, and experimental design including the wind turbine mode, experimental setup and measurements are introduced in Section III. In Section IV, results are presented. First, the statistical analysis, averaged profile and then POD analysis in subsection A-C. Subsequently, in subsection D, the results for Reconstruction averaged profile using a multiple POD modes are discussed. In section V the power mea-

surements are identified and finally, conclusions are presented in Section VI.

II. SNAPSHOT PROPER ORTHOGONAL DECOMPOSITION

Balancing gains and losses in energy can be quantified through the mean kinetic energy budget [21]. One of the main sources in the energy budget is described by the spatial transport of energy by Reynolds shear stress, named the energy flux. The Reynolds shear stress is responsible for the mean kinetic energy flux. This study will focus on the Reynolds shear stress and energy flux to quantify the impact of the streamwise and spanwise spacing through the statistical analysis and using proper orthogonal decomposition. POD is a mathematical tool that derives optimal basis functions from a set of measurements and decomposes the flow into modes that express the most dominant features. This technique, which is presented in the frame of turbulence by Lumley [22], categorizes structures within the turbulent flow depending on their energy content and allows for filtering the structures associated with the low energy level. Sirovich [23] presented the snapshot POD that relaxes the difficulties of the classical orthogonal decomposition. The snapshot method enables reducing POD computational cost when the space dimension of a single snapshot is larger than the total number of snapshots. POD used to describe coherent structures of different types of flow such as axisymmetric mixing layer [24], channel flow [25], atmospheric boundary layer [26], wake behind disk [27], and subsonic jet [28]. In the frame of a wind turbine wake flow, Andersen et al. [29] applied POD to the flow in a wind farm simulated using LES. It was shown that the large scale motion and dynamic wake meandering are strongly governed by turbine spacing. The number of modes required to reconstruct the flow proportional to the homogeneity of the input snapshots. Hamilton et al. [30] investigated the wake interaction and recovery dynamics for Cartesian and row-offset wind arrays, showing that the flux of turbulence kinetic energy is reconstructed with approximately 1% of the total modes. Bastine et al. [31] performed analysis for a single wind turbine modeled *via* LES, observing the three modes is sufficient to capture the dynamic of the effective velocity over a potential disk. Recently,

VerHulst and Meneveau [32] applied three dimensional POD on the LES data and quantified the contribution of each POD mode to the energy entrainment, finding that the net entrainment is relevant to the layout of the wind turbines in the field.

The flow field, taken as the fluctuating velocity, can be represented as $u = u(\vec{x}, t^n)$, where $\vec{x}$ and t^n refer to the spatial coordinates and time at sample n, respectively. A set of the orthonormal basis functions, ϕ, can be presented as

$$\phi_i = \sum_{n=1}^{N} A(t^n) u(\vec{x}, t^n). \tag{1}$$

The optimal functions have minimum averaged error and maximum averaged projection in mean square sense. The largest projection can be determined using the two point correlation tensor and Fredholm integral equation

$$R(\vec{x}, \vec{x}^{'}) = \frac{1}{N} \sum_{n=1}^{N} u(\vec{x}, t^n) u^T(\vec{x}^{'}, t^n), \tag{2}$$

$$\int_{\Omega} R(\vec{x}, \vec{x}^{'}) \phi(x^{'}) dx^{'} = \lambda \phi(x), \tag{3}$$

where $R(\vec{x}, \vec{x}^{'})$ is a spatial correlation between two points $\vec{x}$ and $\vec{x}^{'}$, N is the number of snapshots, T is the transpose of the matrix, and λ are the eigenvalues. **To acquire the optimal basis functions, the problem is reduced to the eigenvalue problem denoted,**

$$[C][G] = \lambda[G]. \tag{4}$$

where $\boldsymbol{C}$, $\boldsymbol{G}$ and λ are the correlation tensor, basis of eigenvector, and the eigenvalues matrix, respectively. The eigenfunctions are orthogonal and the corresponding eigenvalues are positive and real, and organized in descending order. The POD eigenvectors illustrate the spatial structure of the turbulent flow and the eigenvalues measure the energy associated with corresponding eigenvectors. The summation of the eigenvalues presents the total turbulent kinetic energy (E) in the flow domain. The fraction of the cumulative energy, η and the normalized energy content of each mode, ξ, can be represented as,

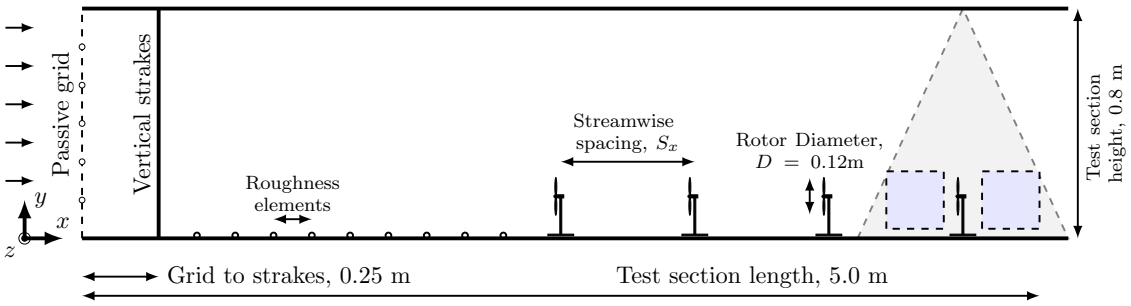

FIG. 1: Experimental Setup. Dashed gray lines indicate the placement of the laser sheet relative to the model wind turbine array. Filled gray boxes indicate measurement locations discussed below.

$$\eta_n = \frac{\sum_{n=1}^{n} \lambda_n}{\sum_{n=1}^{N} \lambda_n}, \tag{5}$$

$$\xi_n = \frac{\lambda_n}{\sum_{n=1}^{N} \lambda_n}. \tag{6}$$

POD tool is particularly useful in rebuilding the Reynolds shear stress using a set of eigenfunctions as follows,

$$\langle u_i u_j \rangle = \sum_{n=1}^{N} \lambda_n \phi_i^n \phi_j^n. \tag{7}$$

III. EXPERIMENTAL DESIGN

A 4×3 array of wind turbines was placed in the closed- circuit wind tunnel at Portland State University to study the effects due to variation in streamwise and spanwise spacing in a wind turbine array. The dimensions of the wind tunnel test section are 5 m (long), 1.2 m (wide) and 0.8 m (height). The entrance of the test section is conditioned by the passive grid, which consists of 7 horizontal and 6 vertical rods, to introduce large-scale turbulence. **Nine vertical Plexiglas strakes located at 0.25 m downstream of the passive grid and 2.15 m upstream of the first row of the wind turbine were used to modify the inflow.** The thickness of the strakes is 0.0125 m with a spanwise spacing of 0.136 m. Surface roughness elements were placed on the wall as a series of chains with a diameter of 0.0075 m and spaced 0.11 m apart. Figure 1 shows the schematic of the experimental setup.

Sheet steel of 0.0005 m thick was used to construct the 3 bladed wind turbine rotors. The diameter of the rotor was $D = 0.12$ m, equal to the height of the turbine tower. Each rotor blade was pitched at 15° out of a plane at the root and 5° at the tip. These angles were chosen to provide angular velocity that correlates with required ranges of tip-speed ratio. A DC electrical motor of 0.0013 m diameter and 0.0312 m long formed the nacelle of the turbine and was aligned with the flow direction. A torque sensing system was connected to the DC motor shaft following the design outlined in [33]. Torque sensor consists of a strain gauge, Wheatstone bridge and the Data Acquisition with measuring software to collect the data. For more information on the experiment conditions and data processing, see [20].

In this study, the flow field was sampled under neutral stratification in four configurations of a model-scale wind turbine array, classified as $C_{S_x \times S_z}$, and considered in Table I. Permutations of the streamwise spacing (S_x) of $6D$ and $3D$ and spanwise spacing (S_z) of $3D$ and $1.5D$ are examined. Thus, the four cases present aligned wind farm; the staggered wind farm does not consider in this study. Stereoscopic particle image velocimetry (SPIV) was used to measure streamwise, wall-normal and spanwise instantaneous velocity at the upstream and downstream of the wind turbine at the center line of the fourth row as shown in figure 2. At each measurement location, 2000 images were taken, to ensure convergence of second-order statistics. **SPIV equipment is LaVision and consists of a Nd:Yag (532nm, 1200mJ, 4ns duration) double-pulsed laser and four 4 MP ImagerProX CCD cameras positioned for the upstream and downstream of the wind turbine.** Neutrally buoyant fluid particles of diethyl hexyl sebacate were introduced to the flow and allowed to mix. Consistent seeding density was maintained in order to mitigate measurement errors. The laser sheet of 0.001 m thick with less than 5 mrad divergence angle is positioned and the measurement windows are 0.2 m × 0.2 m. A multi-pass fast Fourier transformation was used to process the raw data into vector fields. Erroneous measurement of the vector fields were replaced using Gaussian interpolation of neighboring vectors.

TABLE I: Streamwise and spanwise spacing of the experimental tests.

Cases	S_x	S_z	Occupied Area
$C_{6\times3}$	$6D$	$3D$	$18D^2$
$C_{3\times3}$	$3D$	$3D$	$9D^2$
$C_{3\times1.5}$	$3D$	$1.5D$	$4.5D^2$
$C_{6\times1.5}$	$6D$	$1.5D$	$9D^2$

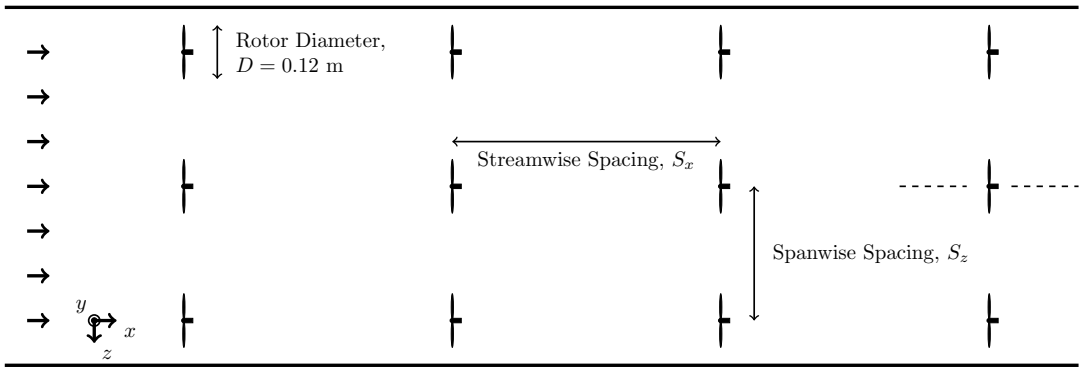

FIG. 2: Top view of 4 by 3 wind turbine array. The dash lines at the last row centerline turbine represent the measurement locations.

IV. RESULTS

A. Statistical Analysis.

Herein, characterization of the wind turbine wake flow is presented by streamwise mean velocity, Reynolds shear stress, and energy flux, with the aim to comprehend the influence of turbine-to-turbine spacing. Figure 3 presents the normalized streamwise velocity, U/U_h, in upstream and downstream of the cases $C_{6\times3}$, $C_{3\times3}$, $C_{3\times1.5}$ and $C_{6\times1.5}$, where U_h is the inflow velocity at hub height of case $C_{6\times3}$ that is used to normalize the velocities of the four considered cases. The left and right contours of each case present the upstream and downstream flow, respectively. At upstream, case $C_{6\times3}$ attains the largest streamwise mean velocities compared with the other cases due to greater recovery of the flow upstream of the turbine. Although the streamwise spacing of case $C_{6\times1.5}$ is similar to case $C_{6\times3}$, the former shows reduced hub height velocity. The normalized mean velocity is about 0.567 compared with 0.66 in case $C_{6\times3}$, confirming

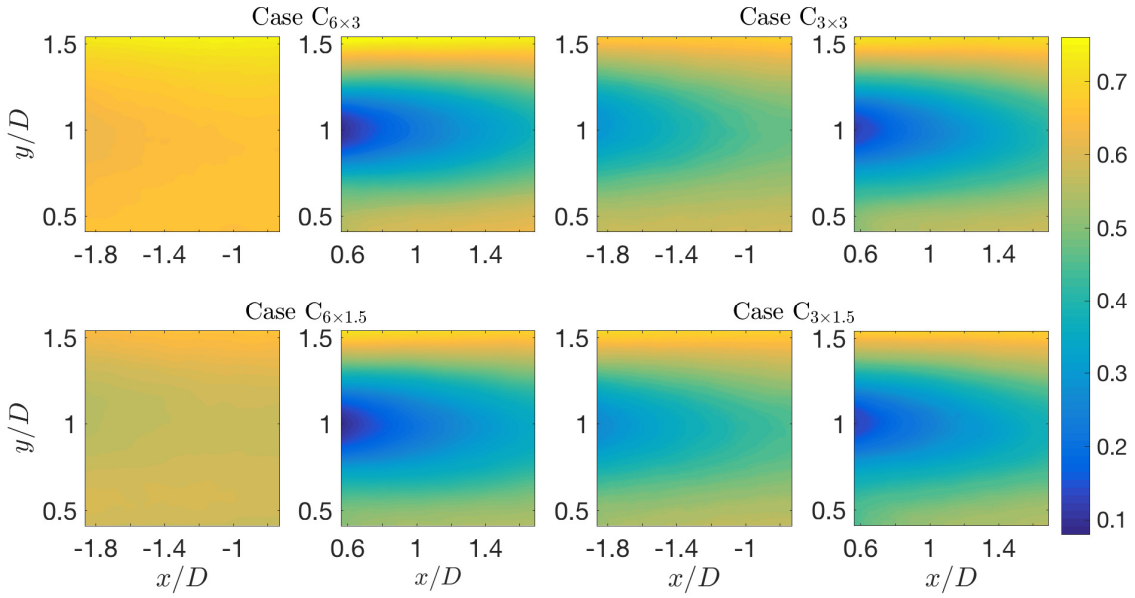

FIG. 3: Normalized streamwise velocity, U/U_h, at upstream and downstream of the cases $C_{6\times3}$, $C_{3\times3}$, $C_{3\times1.5}$, and $C_{6\times1.5}$.

the influence of the spanwise spacing on wake evolution and flow recovery. Small variations are perceived between case $C_{3\times3}$ and $C_{3\times1.5}$ above the top tip ($y/D = 1.5$) and below the bottom tip ($y/D = 0.5$), where case $C_{3\times3}$ demonstrates higher velocities. Downstream of the turbine, the four cases expose clear differences especially above the top tip and below the bottom tip, where case $C_{6\times3}$, once again, shows the greatest velocities. Case $C_{3\times3}$ also shows higher velocities below the bottom tip compared with cases $C_{3\times1.5}$ and $C_{6\times1.5}$. **The comparison between case $C_{3\times1.5}$ and case $C_{6\times1.5}$ shows a resemblance in velocity distribution with the exception at region $x/D < 0.8$, where case $C_{6\times1.5}$ displays the most significant velocity deficit. The normalized mean streamwise velocity as well as turbulence intensity in Nilsson et al. [12] shows the compound wakes from the upstream and downstream turbines and that confirms the current result of cases $C_{3\times3}$ and $C_{3\times1.5}$. Furthermore, in the row where a turbine is not present, the flow is provided the opportunity to recover as it is the case in this study, that is, similar to the cases $C_{6\times3}$ and $C_{6\times1.5}$.**

Figure 4 comprises the in-plane Reynolds shear stress $-\langle uv \rangle$ for the same cases as shown in figure 3, where u and v is the fluctuating velocity in streamwise and wall-normal direction, respectively. At upstream, cases $C_{3\times3}$ and $C_{3\times1.5}$ display higher stress compared with $C_{6\times3}$

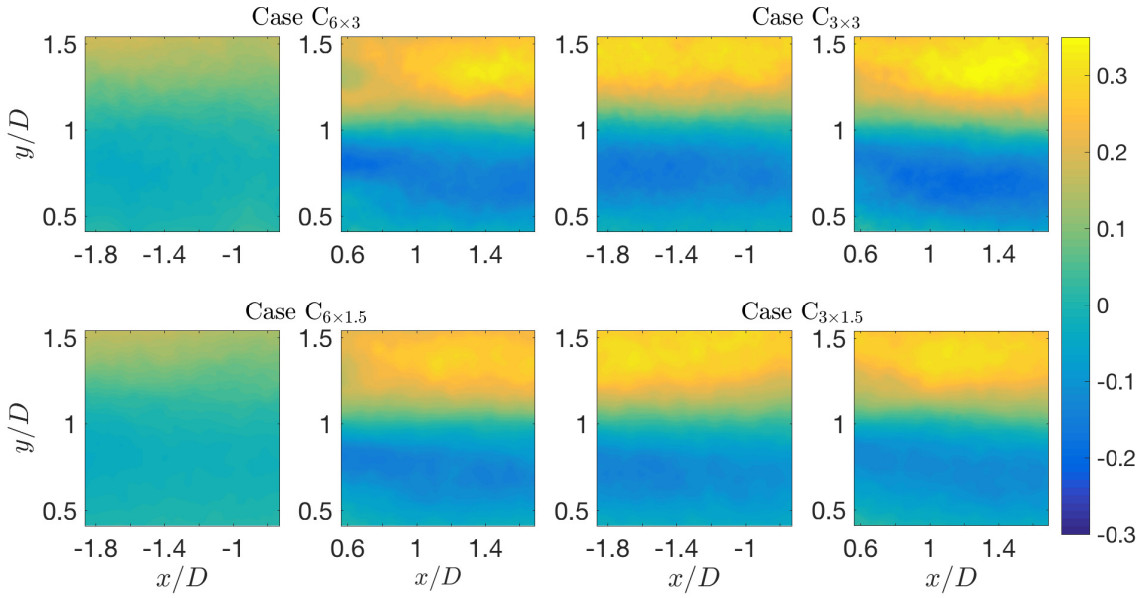

FIG. 4: Reynolds shear stress, $-\langle uv \rangle$, in upstream and downstream of the each measurement case.

and $C_{6\times1.5}$. Although the spanwise spacing of case $C_{3\times1.5}$ is half of case $C_{3\times3}$, no vital difference is apparent. **The differences are clear at** $0.5 \leq y/D \leq 1$**, where case** $C_{3\times3}$ **exhibits heightened magnitudes of** $-\langle uv \rangle$**.** At the downstream, comparison between the cases indicates that reducing streamwise spacing increases the Reynolds shear stress. This difference is clearly discerned comparing cases $C_{6\times1.5}$ and $C_{6\times3}$ at $x/D \geq 1$. The average over the downstream domain shows increasing of 16% in Reynolds shear stress of case $C_{3\times3}$. A similar effect is observed in case $C_{3\times1.5}$ where it exhibits higher stress than case $C_{6\times1.5}$ with increasing average of 2% is noticed. The effect of spanwise spacing is more apparent when the streamwise spacing is $3D$ as can be seen when comparing between case $C_{3\times1.5}$ and case $C_{3\times3}$, which shows an increase of 20% on average over the domain. However, decreasing spanwise spacing increases $-\langle uv \rangle$ slightly as shown when comparing between case $C_{6\times3}$ and $C_{6\times1.5}$. The difference of 6% is shown and the variation is observed only in a small region at ($y/D \approx 1.3$ and $x/D > 1.2$), where higher Reynolds shear stress is found in case $C_{6\times3}$.

Figure 5 displays the vertical flux of kinetic energy, $-\langle uv \rangle U$. At upstream, a small disparity is shown between case $C_{6\times3}$ and $C_{6\times1.5}$, it is mainly above the top tip as a consequence of the higher mean velocity of the case $C_{6\times3}$ at this location. The maximum $-\langle uv \rangle U$ is found at case $C_{3\times3}$ and $C_{3\times1.5}$. The variation between cases $C_{3\times3}$ and $C_{3\times1.5}$ shows that maximum negative flux is detected in the regions between the hub height and bottom tip of the case

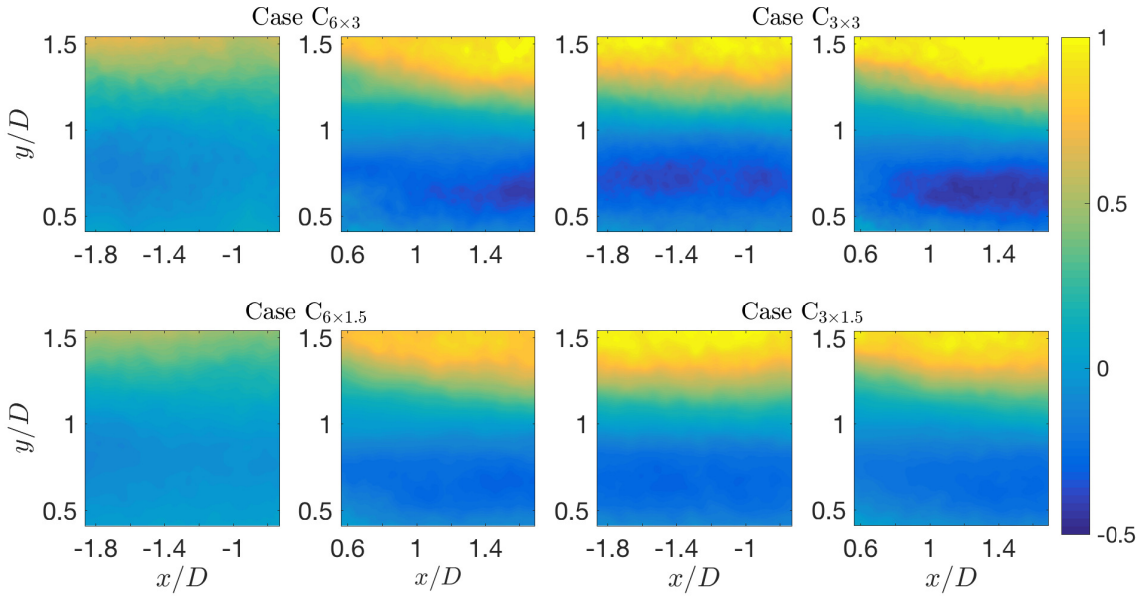

FIG. 5: Flux of kinetic energy, $-\langle uv\rangle U$, in upstream and downstream of the each measurement case.

$C_{3\times3}$; higher positive flux is located above the top tip of the case $C_{3\times1.5}$. At downstream, case $C_{6\times3}$ displays the same energy flux distribution of case $C_{6\times1.5}$ with significant differences in the regions of $x/D > 1.3$, where case $C_{6\times3}$ demonstrates higher energy flux. The average value over the downstream domain shows a decrease of 14% in $-\langle uv\rangle U$ in case $C_{6\times1.5}$. The same tendency is observed when comparing between cases $C_{3\times3}$ and $C_{3\times1.5}$, decreasing about 24.5% in the vertical flux. This result verifies that when the spanwise spacing decreases, the energy flux decreases also. Decreasing the streamwise spacing, case $C_{3\times3}$ exhibits higher $-\langle uv\rangle U$ than case $C_{6\times3}$ mainly when $x/D > 1$, where the average value over the domain increases by 15%. Similar behavior is observed when comparing between case $C_{3\times1.5}$ and $C_{6\times1.5}$. Case $C_{3\times1.5}$ displays an increase in $-\langle uv\rangle U$ of 5% over case $C_{6\times1.5}$ and the main differences are seen at $x/D > 1$ and $y/D \approx 1.5$. In general, the impact of streamwise spacing on energy flux is more pronounced when spacing $z = 3D$ than $1.5D$. The impact of spanwise spacing on energy flux is more pronounced when the spacing $x = 3D$ than $6D$. Overall, case $C_{3\times3}$ shows the highest values of $-\langle uv\rangle U$ comparing with other cases.

B. Averaged Profiles.

Spatial averaging of the variables is determined by moving the upstream domain of each case beyond its corresponding downstream flow and performing streamwise averaging according to the procedure adopted in Cal *et al.* [3]. Spatial averaging makes it possible to compare the different cases while removing the streamwise dependence. Here, streamwise averaging is denoted by $\langle\cdot\rangle_x$. Figure 6(a) shows profiles of streamwise-averaged mean velocity for all four cases. Case $C_{6\times3}$ and case $C_{3\times1.5}$ show the largest and smallest velocity deficits, respectively. At hub height, the velocity of the case $C_{6\times3}$ is approximately 2.25 ms^{-1} whereas case $C_{3\times1.5}$ shows approximately velocity of 1.6 ms^{-1}. The difference between case $C_{6\times3}$ with case $C_{6\times1.5}$ is less than the difference between case $C_{6\times3}$ with case $C_{3\times3}$ confirming that the impact of reducing streamwise spacing is greater than changing the spanwise spacing. The influence of streamwise spacing is also observed when comparing cases $C_{3\times1.5}$ and $C_{6\times1.5}$. Interestingly, a reduction in streamwise spacing show less effect when the spanwise spacing $z/D = 1.5$. For example, the maximum disparity in streamwise velocity between the cases $C_{6\times3}$ and $C_{3\times3}$ is 0.57 ms^{-1}, in contrast to the dissimilarity of 0.42 ms^{-1} between cases $C_{3\times1.5}$ and $C_{6\times1.5}$. Trivial variations are noted between the profiles of cases $C_{3\times3}$ and $C_{3\times1.5}$. The cases $C_{3\times3}$, $C_{3\times1.5}$ and $C_{6\times1.5}$ converge at $y/D > 1.4$ while the case $C_{3\times3}$ and case $C_{3\times1.5}$ combine at the regions above the hub height.

Figure 6(b) contains the streamwise-averaged Reynolds shear stress $-\langle uv\rangle$ for cases $C_{6\times3}$ through $C_{6\times1.5}$. Slight decreasing in $-\langle uv\rangle$ is attained in case $C_{6\times1.5}$, where the spanwise spacing is reduced. Reducing spanwise spacing shows an important influence when the streamwise spacing is $x/D = 3$. The discrepancies between case $C_{3\times3}$ and case $C_{3\times1.5}$ are greatest in the region below hub height. The streamwise spacing plays a larger role than the spanwise spacing, *e.g.*, the maximum differences between the Reynolds shear stress profiles are detected between case $C_{6\times3}$ and case $C_{3\times3}$. Interestingly, the largest difference between the Reynolds shear stress of cases is found between case $C_{6\times3}$ and case $C_{3\times3}$, located at $y/D \approx 0.7$ and $y/D \approx 1.4$. Furthermore, the four cases have approximately zero Reynolds shear stress at the inflection point located at hub height. In addition, the most striking result to emerge from averaged profiles is that case $C_{3\times3}$ displays the maximum Reynolds stress and case $C_{6\times1.5}$ presents the minimum stress.

Figure 6(c) presents the streamwise-averaged profile of the vertical flux of kinetic energy.

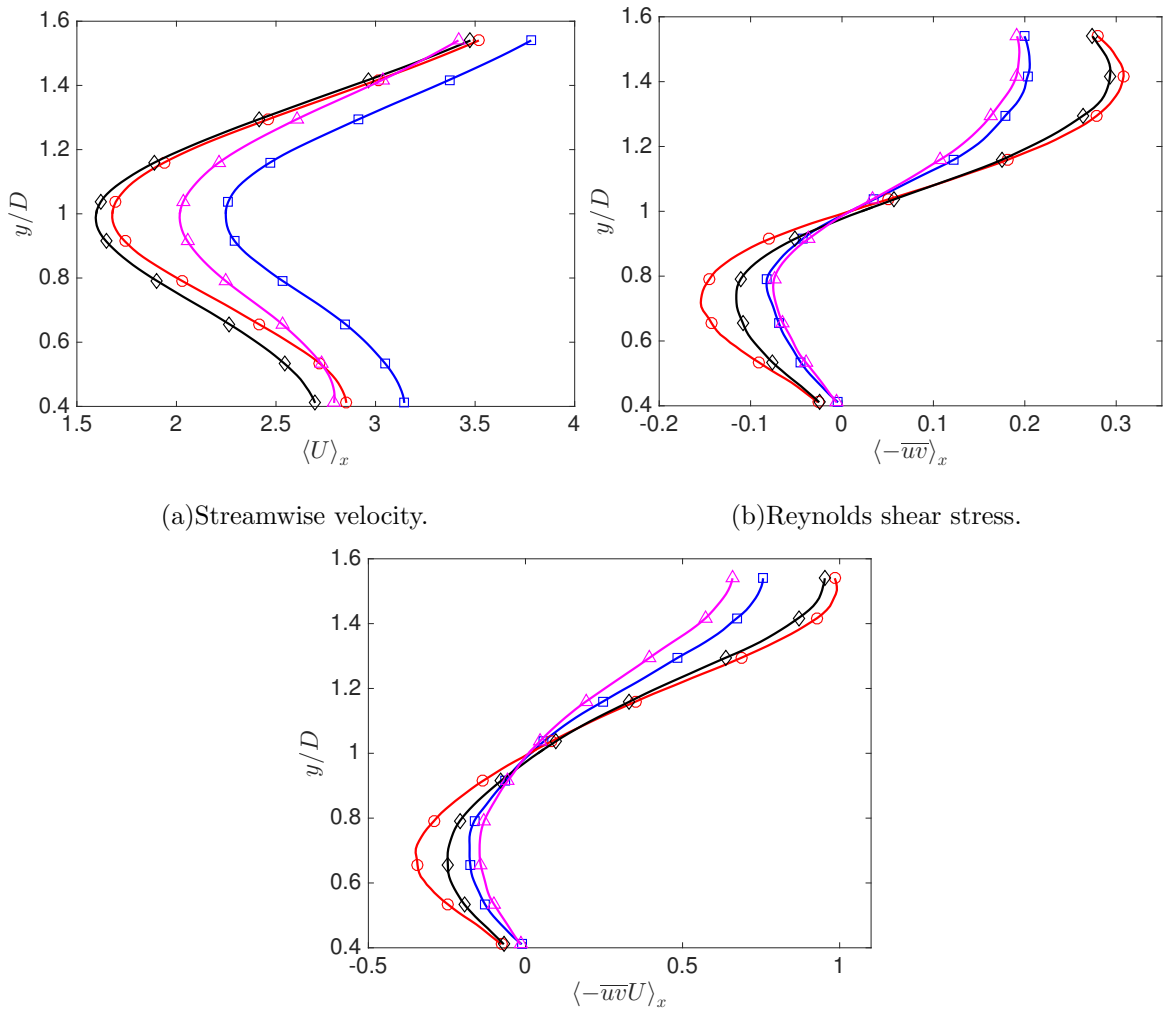

(a)Streamwise velocity.

(b)Reynolds shear stress.

(c)Energy flux

FIG. 6: Streamwise average profile of streamwise velocity, Reynolds shear stress, and energy flux and turbulent for four different cases $C_{6\times3}$ (□), $C_{3\times3}$ (◯), $C_{3\times1.5}$ (◊), and $C_{6\times1.5}$ (△).

Below the hub height, the difference cases $C_{6\times3}$ and $C_{6\times1.5}$ is small. The variation begins above the hub height and increases with increasing wall-normal distance due to the variation of the streamwise velocity of these two cases as shown in figure 6(a). The significant variations between case $C_{3\times3}$ and $C_{3\times1.5}$ are observed below the hub height due to the significant difference between the Reynolds shear stress of these two cases as can be shown in figure 6(b). Above the hub height, the difference between these cases is diminished. In general, when spanwise spacing decreases, the energy flux also decreases as shown when comparing between case $C_{6\times3}$ with case $C_{6\times1.5}$ and case $C_{3\times3}$ with case $C_{3\times1.5}$. In contrast, when streamwise spacing decreases the vertical flux of kinetic energy increases per unit streamwise

spacing. The maximum and minimum flux are observed at case $C_{3\times3}$ and case $C_{6\times1.5}$, respectively. The region that is near to the hub height also shows zero energy flux and changes the sign of the energy flux.

C. Proper Orthogonal Decomposition.

Based on the velocity field, the spatially integrated turbulent kinetic energy is expressed by the eigenvalue of each POD mode. Normalized cumulative energy, η_n, from equation (5) for upstream and downstream measurement windows are presented in figure 7(a) and (b), respectively. The insets of the figures exhibit the normalized energy content per mode, ξ_n, which is presented by equation (6). Upstream of the turbine, case $C_{6\times3}$ and case $C_{6\times1.5}$ converge faster than case $C_{3\times3}$ and $C_{3\times1.5}$, respectively. These results are attributed to the reduction the streamwise spacing. Convergence of case $C_{6\times3}$ oscillates around the curve of the case $C_{6\times1.5}$. The same trend is observed between case $C_{3\times3}$ and $C_{3\times1.5}$ but with fewer alternations. Modes 2 through 5 and modes 40 through 100 coincide in cases Π_1 and Π_4. Thus, the convergence of case $C_{3\times3}$ is approximately coincident with case $C_{3\times1.5}$ except at mode 1 and modes 3 through 20. The inset of figure 7(a) shows that the first mode of the case $C_{6\times1.5}$ and case $C_{3\times1.5}$ contain a higher energy content than the first mode of the case $C_{6\times3}$ and case $C_{3\times3}$, respectively. The second mode of case $C_{6\times1.5}$ shows a greater decrease in energy content from mode one than case $C_{6\times3}$, accounting for the convergence profile of cases $C_{6\times3}$ and case $C_{6\times1.5}$ at mode 2. The energy content, ξ_n, shows a trivial difference, $\mathcal{O}(10^{-3})$, between the four cases after mode 10. For the downstream flow, case $C_{6\times1.5}$ converges faster than the other cases, thereafter it is ordered as Π_1, Π_2 and Π_3 in succession. The oscillating behavior observed in the upstream flow, is noticed only between case $C_{3\times3}$ and $C_{3\times1.5}$. Beyond the tenth mode, the difference in energy content among the four cases is negligible.

The comparison between the upstream and downstream reveals that energy accumulates in fewer modes in the upstream of each case, *e.g.*, case $C_{6\times3}$ requires 14 modes to obtain 50% of the total kinetic energy in upstream, whereas 26 modes are required to obtain the same percentage of energy downstream. Greater dissimilarity is observed between the convergence of cases $C_{6\times3}$ and $C_{6\times1.5}$ at the downstream than the difference at the upstream. The contrast between case $C_{6\times3}$ and $C_{6\times1.5}$ is larger than the discrepancy between case $C_{3\times3}$

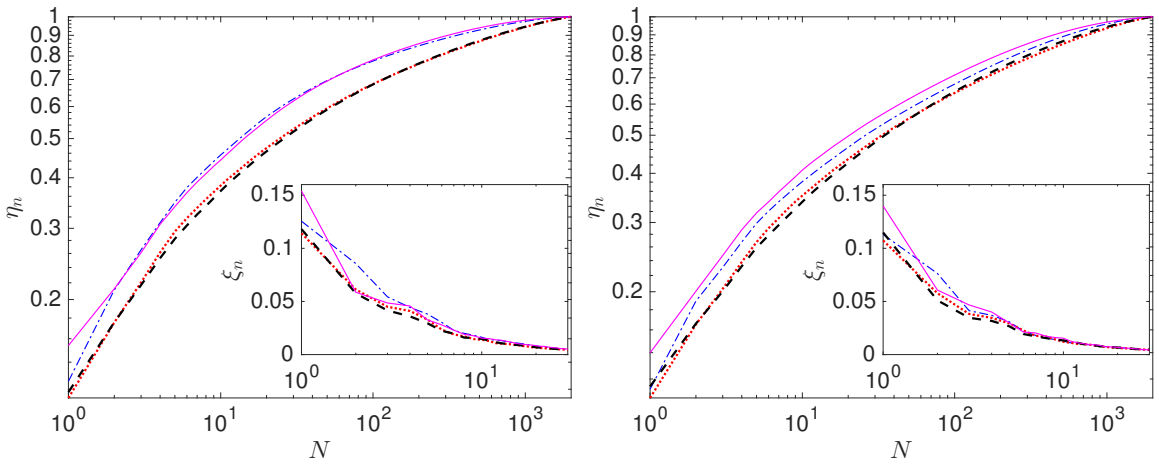

(a)Upstream. (b)Downstream.

FIG. 7: Energy content of the POD modes for four different cases: $C_{6\times3}$ ($-\cdot-$), $C_{3\times3}$ ($\cdots$), $C_{3\times1.5}$ ($--$), and $C_{6\times1.5}$ ($-$).

and $C_{3\times1.5}$ especially at downstream. The disparity between the upstream and downstream windows can be identified in the most energetic mode that shows the maximum and minimum variations at case $C_{6\times1.5}$ and case $C_{3\times1.5}$, respectively. This observation can be attributed to the structure of the upstream flow of case $C_{6\times1.5}$ that is rather recovered, whereas the downstream show a high deficit. However, the upstream and downstream of the case $C_{3\times1.5}$ both show a high velocity deficit, therefore the structure might be similar especially for large scale. From mode 2 through 10, the biggest difference between the upstream and downstream is found in case $C_{6\times3}$. With the maximum spacing area per turbine, the flow is expected to become more homogeneous in the upstream window and exhibit the most significant momentum deficit in the wake, accounting for the differences seen in η_n upstream and downstream.

Figure 8 presents the first POD mode at the upstream and downstream of the considered cases. The four cases show that small gradients in the streamwise direction compared to a high gradient in the wall-normal direction. Although the four cases show a divergence between the eigenvalues of the first mode, the eigenfunctions display fairly similar structures. The energy of the first POD mode shows a variation of 1.25% when comparing between the upstream and downstream of the case $C_{6\times3}$. Less variations of 0.68% and 0.32% are observed in the cases $C_{3\times3}$ and $C_{3\times1.5}$, respectively. Consequently, the structures of upstream and downstream of these cases are approximately equivalent. The similarity is observed between

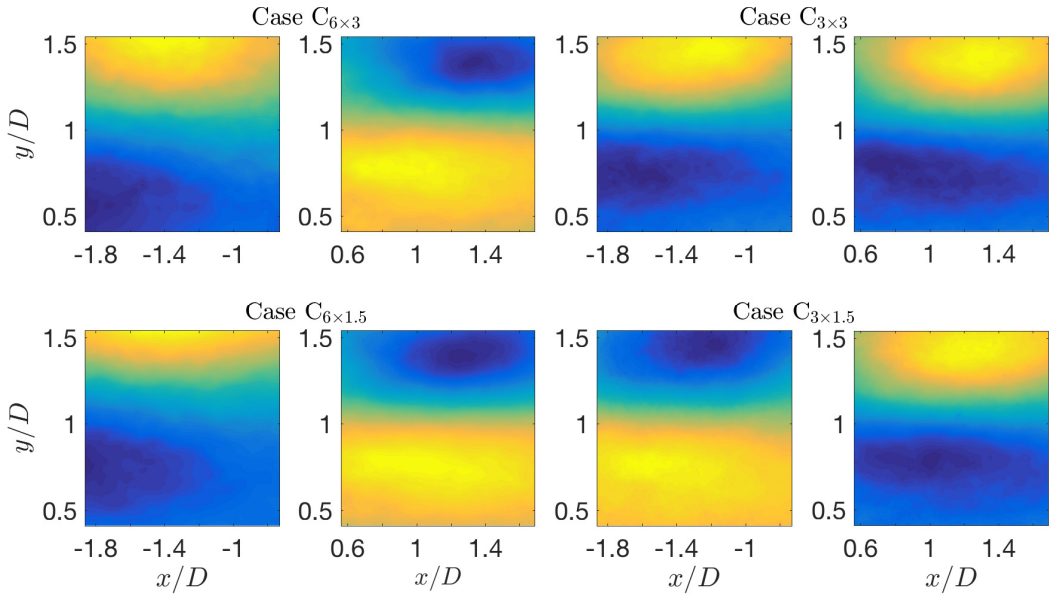

FIG. 8: The first mode at upstream and downstream of the each case.

case $C_{6\times3}$ and $C_{6\times1.5}$ despite the energy difference between them about 3%. Case $C_{6\times1.5}$ presents significant differences between the upstream and downstream mainly at $y/D \approx 1.5$ and the region between the hub height and bottom tip.

Figure 9 presents the fifth POD mode at the upstream and downstream of the four cases that show a combination of POD and Fourier (homogenous) modes in the streamwise direction. Although the fifth mode of the four cases contains $\approx$ 74% less energy of than the first mode, large scales are still pronounced. Small scales also appear in the upstream and the downstream windows. Upstream window of cases Π_1, Π_2, and Π_3 shows shifting of 90 degree in phase angle of structure of its own downstream windows. Interestingly, the upstream and downstream widows of case Π_3 look like the reduced scale of it own first mode. The same trend is observed in the downstream window of the case Π_4.

Figure 10 presents the twentieth mode at the upstream and downstream of the four cases. The small structures become noticeable in both upstream and downstream windows. The upstream of cases $C_{6\times3}$ and $C_{6\times1.5}$ show large scale structure compared with the other two cases. Although, after mode 10, there is no significant difference in the energy content of the cases as shown in figure 6, the structure of the mode shows a significant discrepancy. This observation somewhat surprising and will confirm that the intermediate modes associate with the inflow characterizations.

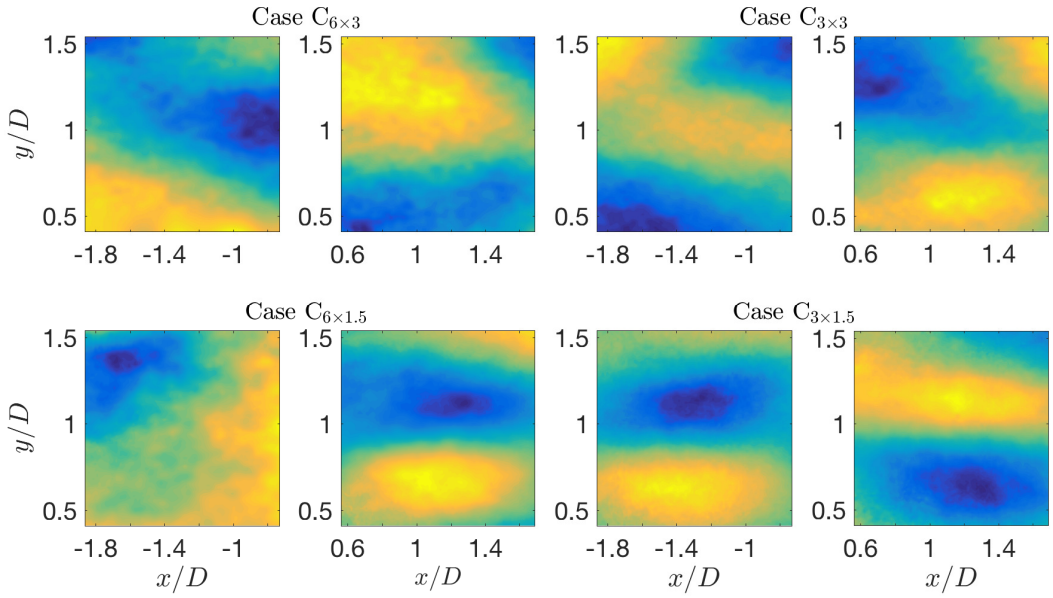

FIG. 9: The fifth mode at upstream and downstream of the each case.

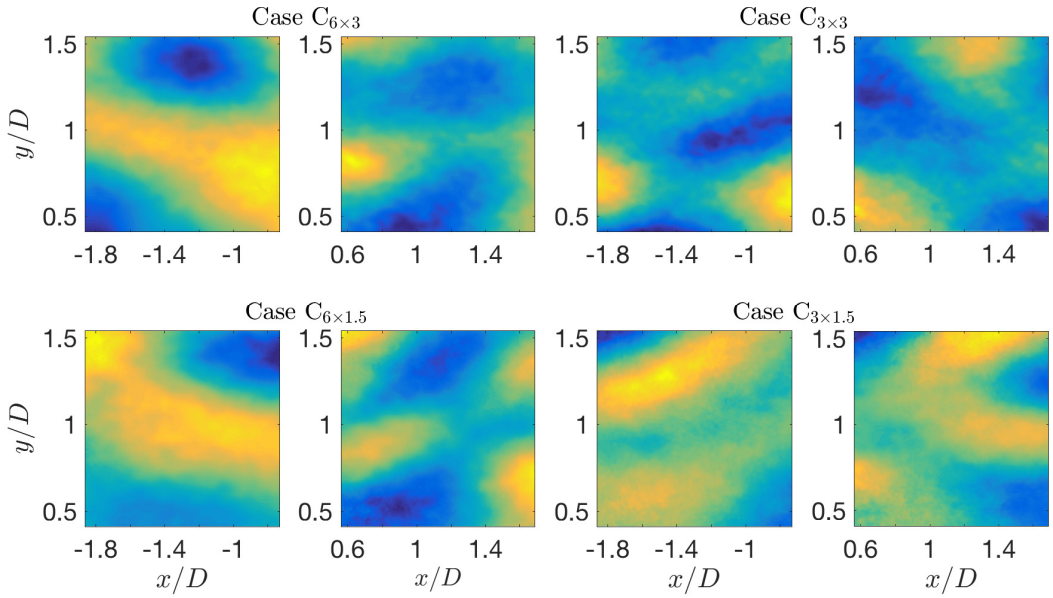

FIG. 10: The twentieth mode at upstream and downstream of the each case.

D. Reconstruction Averaged Profile.

Streamwise-averaged profiles of Reynolds shear stress are reconstructed according to equation (7). Partial amounts of the turbulent kinetic energy are considered using a few modes to reconstruct the stress. In this study, the first mode, the first 5, 10, 25, and 50 modes are used

to reconstruct the stress as shown in figure 11. The inset of the figure presents the Reynolds shear stress construction using the modes 5-10, 5-25, and 5-50, respectively. The black lines are the streamwise average of full data from figure 6(b). Using an equal number of modes, case $C_{6\times1.5}$ rebuilds the profiles of the Reynolds shear stress faster than the other cases. The case $C_{6\times3}$ also shows the fast reconstruction and the dissimilarity with case $C_{6\times1.5}$ is mainly in the profile of first mode (red line) and the first five modes (blue line). The cases $C_{3\times3}$ and $C_{3\times1.5}$ show approximately the same trends in reconstruction profiles. Below hub height, the four cases show the same trend of the first mode profiles, where the contribution in the reconstruction profiles is zero. The first five modes display exactly the form of the full data profile of individual case. The maximum difference between the successive reconstruction profiles displays between the first mode and profile resulting from the first five modes. The cases $C_{6\times3}$, $C_{3\times3}$ and $C_{3\times1.5}$ show a moderate variation between the profiles resulting from first five and first ten (red and green lines, respectively). After the profiles resulting from the first ten modes, the contribution in reconstruction is small as shown magenta and gray lines. Using successively more modes leads to more accurate reconstruction. The maximum difference between the full data and the reconstructed profiles is located at $y/D \approx 0.75$ and $y/D \approx 1.4$, where the extrema in $\langle\overline{-uv}\rangle_x$ are located. **Generally, faster reconstruction implies that the flow possesses coherent structures with a greater portion of the total kinetic energy. Consequently, the flow in the case $C_{6\times3}$ and $C_{6\times1.5}$ is occupied by the coherent structures and is less energetic in cases $C_{3\times3}$ and $C_{3\times1.5}$. Thus, the change in spanwise spacing does not show a significant effect on the coherent structure content when the streamwise spacing is $3D$.**

To quantify the contribution of the moderate-scaled structures, Reynolds shear stress is reconstructed using the intermediate modes. As can be shown in the insets of figure 11, the full data profile (black line) is compared with profiles reconstructed from modes 5-10, 5-25, and 5-50 (peach lines). Surprisingly, the intermediate modes in each case approximately take the form of the full data profiles below the hub height. Reconstruction Reynolds shear stress in Case $C_{6\times3}$ and $C_{6\times1.5}$ show minute variations between the successive reconstruction profiles and approximately take the form of vertical lines above the hub height. This trend is opposite to the trend that is shown in the first mode profile. Cases $C_{3\times3}$ and $C_{3\times1.5}$ show a difference between the successive profiles above the hub height. The maximum difference is observed between the reconstructed profiles from modes 5-10 and

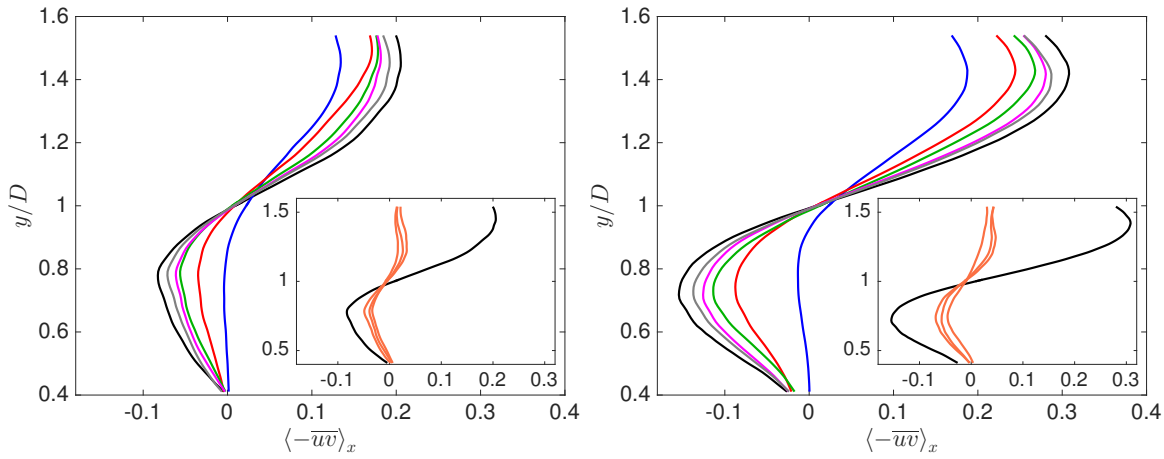

(a)Case $C_{6\times3}$.

(b)Case $C_{3\times3}$.

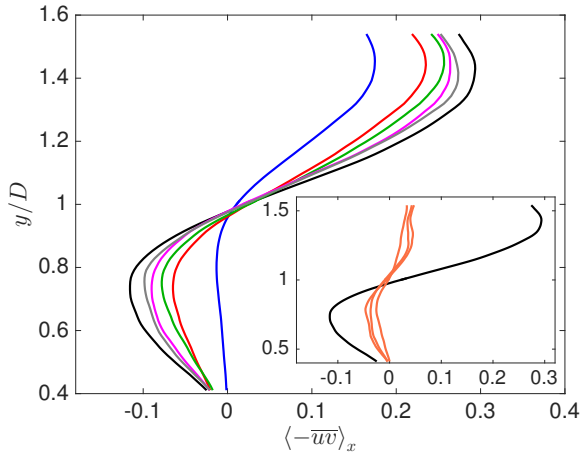

(c)Case $C_{3\times1.5}$.

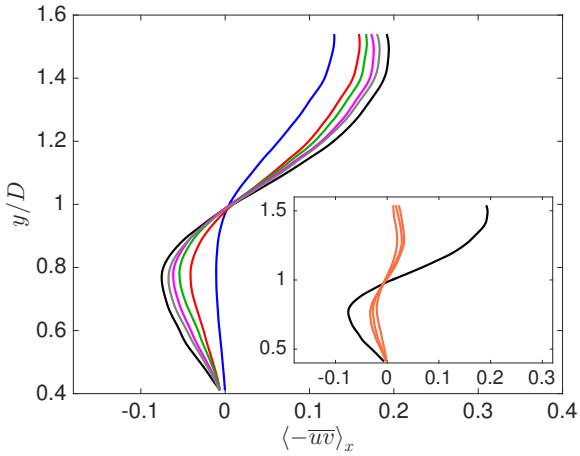

(d)Case $C_{6\times1.5}$.

FIG. 11: Reconstruction Reynolds shear stress using: first mode (—), first 5 modes (—), first 10 modes (—), first 25 modes (—) and first 50 modes (—). Full data statistics (—). The insets show the reconstruction using modes 5-10, 5-25, and 5-50 (—).

from 5-25.

V. POWER MEASUREMENTS.

Figure 12 demonstrates the power produced, $\mathcal{F}_x$, that is obtained directly by the torque sensing system, versus the angular velocity, ω, for all cases. The power measurements are normalized by the maximum theoretical power that is determined by 0.5 $\rho A_c U_\infty^3$, where ρ is the air density, A_c is swept area of the turbine rotor $\pi D^2/4$, and U_∞ is the maximum inflow velocity. The angular

velocity is normalized by the $2U_\infty/D$. It is apparent from the figure that the maximum power is extracted approximately at the normalized angular velocity of 15.8 ± 1. The maximum normalized power of 0.062 is harvested at the largest spacing, *i.e.*, case $C_{6\times3}$. Reducing streamwise spacing shows a significant decrease in extracted power especially at $10.5 < \omega D/2U_\infty < 19$. Fixing spanwise spacing and decreasing the streamwise spacing reduces the normalized power produced by 33% for $S_x = 6D$ (from case $C_{6\times3}$ to case $C_{3\times3}$) and by 22 % for $S_x = 3D$ (from case $C_{3\times1.5}$ to case $C_{6\times1.5}$). The complementary change in spacing holds the streamwise spacing constant while decreasing the spanwise spacing. In that case the normalized power produced is reduced by 20% for $S_z = 3D$ (from case $C_{6\times3}$ to case $C_{6\times1.5}$) and by 6% for $S_z = 1.5D$ (from case $C_{3\times3}$ to case $C_{3\times1.5}$). Nilsson et al. [12] has complementary results to the ones present, where an increase in power produced is attained in the largest spacing and conversely, decreased in the limited spacing case. Furthermore, increasing the spanwise distance has a less notable effect in comparison to the streamwise spacing.

The trend of the power curves follows the same that observed in the averaged profiles of the streamwise velocity, see figure 6 (a). Further, they verify the relationship between the power of the turbine with the deficit velocity. The maximum power and velocity are found in the case $C_{6\times3}$ and the minimum quantities are noticed in $C_{6\times1.5}$. Finally, the smallest variations in the power measurement and main velocity are observed between cases $C_{3\times3}$ and $C_{3\times1.5}$, whereas the largest difference is observed between cases $C_{6\times3}$ and $C_{3\times3}$.

VI. CONCLUSIONS

Insight into the behavior of the flow in a wind turbine array is useful in determining how to highlight the overall power extraction with the variation in spacing between the turbines. The main goal of the current study is to determine the effect of the tight spacings on the flow behavior and the findings of this study have a number of important implications, especially regarding the cost of a wind farm or when the large areas are not available. Stereographic PIV data are used to assess characteristic quantities of the flow field in a wind turbine array with

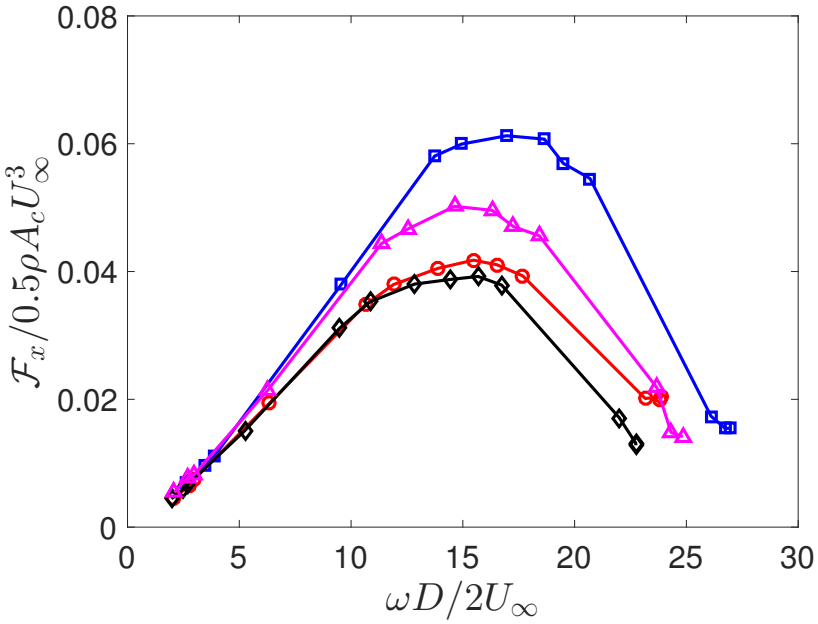

FIG. 12: Extracted power of the wind turbine at different angular velocities for four different cases $C_{6\times3}$ (□), $C_{3\times3}$ (◯), $C_{3\times1.5}$ (◊), and $C_{6\times1.5}$ (△).

varied streamwise and spanwise spacing. Four cases of different streamwise and spanwise spacings are examined; the streamwise spacing being $6D$ and $3D$, and spanwise spacing being $3D$ and $1.5D$. The flow fields are analyzed and compared statistically and by snapshot proper orthogonal decomposition.

Streamwise mean velocity, Reynolds shear stress and vertical energy flux are presented in upstream and downstream of the considered cases. In the inflow measurement window, higher velocities are observed in cases $C_{6\times3}$ and $C_{6\times1.5}$ comparing to the other two cases whose inflows are unrecovered wakes from leading rows. In contrast, case $C_{3\times3}$ and $C_{3\times1.5}$ show higher Reynolds shear stress and energy flux. The notable differences between the cases are found above the top tip and below the bottom tip downstream the turbines, whereas the core of the wakes shows fewer discrepancies. The streamwise and spanwise spacings form a unified effect on the flow, where the degree of the impact of one highly depends on the other. This relation is shown in all statistical quantities such as reducing 50% of the streamwise spacing leads to increase the averaged Reynolds shear stress by 16% and 2% when $z = 3D$ and $1.5D$, respectively. According to current statistical quantities, one can infer that the higher influence

of streamwise spacing is shown when the spanwise spacing is $z = 3D$, and the significant effect of the spanwise spacing is observed when the streamwise spacing is $x = 3D$. In order to remove the streamwise dependence, streamwise average profiles of the statistical quantities are computed. Averaged profiles of the velocity follow the order of higher velocity seen in the contour plots in case $C_{6\times3}$ and lowest velocity in case $C_{3\times1.5}$. The maximum and minimum difference are observed between cases $C_{6\times3}$ with case $C_{3\times1.5}$ and $C_{3\times3}$ with case $C_{3\times1.5}$. The result also reveals that the streamwise spacing is more impactful than the spanwise spacing. Averaged profile of Reynolds shear stress and energy flux shows the same sequence where the maximum and minimum locate in case $C_{3\times3}$ and case $C_{6\times1.5}$, respectively.

Based on the POD analysis, the upstream of the four cases converges faster than the downstream flow. Case $C_{6\times3}$ and $C_{6\times1.5}$ show the rapid convergence in cumulative energy content in upstream, in contrast, case $C_{6\times3}$ remains behind case $C_{6\times1.5}$ in the downstream. The first mode of the case $C_{6\times1.5}$ carries the maximum turbulent kinetic energy content compared to the first mode of the other cases. No significant difference in energy content is observed after the mode 10 between the four cases. The streamwise-averaged profiles of the Reynolds shear stress are reconstructed by back-projecting coefficients onto the set of eigenfunctions. Low index modes are used individually to show the POD mode contributions. Cases $C_{6\times1.5}$ and $C_{6\times3}$ rebuild the average profile faster than other two cases and the discrepancy in reconstruction between them is mainly observed in profiles using only the first five modes. The same trend in reconstruction is observed in cases $C_{3\times3}$ and $C_{3\times1.5}$. The reconstructed profiles display the effect of the spacing and the variation between the wind array, where the array of large streamwise spacing exceeds and reconstruct faster than the other cases due to carrying more coherent structure within the flow.

Power produced is measured directly using torque sensing system. The power curves exactly follow the trend of the velocity profiles. The maximum power extracted at the normalized angular velocity of 15.8 ± 1 and it is harvested in case $C_{6\times3}$. The small difference in harvested power is observed between cases $C_{3\times3}$ and $C_{3\times1.5}$. The current work demonstrates that the wake statistics and

power produced by a wind turbine depend more on streamwise spacing than spanwise spacing. However, the results above pertain only to a fixed inflow direction. In the case where the bulk flow orientation changes, spacing in both the streamwise and spanwise directions will be important to the optimal power production in a wind turbine array. These current results are in agreement with the LES study by Nilsson et al. [12]. Continued efforts are required to understand the impact of streamwise and spanwise spacing in infinite array flow with different stratification conditions.

Acknowledgments

The authors are grateful to NSF-ECCS-1032647 for funding this research.

---

[1] R. J. Barthelmie, S. T. Frandsen, M. Nielsen, S. Pryor, P.-E. Rethore, and H. Jørgensen, Wind Energy **10**, 517 (2007).

[2] L. P. Chamorro and F. Porté-Agel, Boundary-layer meteorology **132**, 129 (2009).

[3] R. B. Cal, J. Lebrón, L. Castillo, H. S. Kang, and C. Meneveau, Journal of Renewable and Sustainable Energy **2**, 013106 (2010).

[4] M. Calaf, C. Meneveau, and J. Meyers, Physics of Fluids **22**, 015110 (2010).

[5] L. P. Chamorro and F. Porté-Agel, Energies **4**, 1916 (2011).

[6] R. J. Barthelmie, S. Pryor, S. T. Frandsen, K. S. Hansen, J. Schepers, K. Rados, W. Schlez, A. Neubert, L. Jensen, and S. Neckelmann, Journal of Atmospheric and Oceanic Technology **27**, 1302 (2010).

[7] R. J. Barthelmie and L. Jensen, Wind Energy **13**, 573 (2010).

[8] K. S. Hansen, R. J. Barthelmie, L. E. Jensen, and A. Sommer, Wind Energy **15**, 183 (2012).

[9] F. González-Longatt, P. Wall, and V. Terzija, Renewable Energy **39**, 329 (2012).

[10] J. Meyers and C. Meneveau, Wind Energy **15**, 305 (2012).

[11] R. J. Stevens, Wind Energy p. 10.1002/we.1857 (2015).

[12] K. Nilsson, S. Ivanell, K. S. Hansen, R. Mikkelsen, J. N. Sørensen, S.-P. Breton, and D. Henningson, Wind Energy **18**, 449 (2015).

[13] J. Meyers and C. Meneveau, AIAA **827**, 2010 (2010).

[14] X. Yang, S. Kang, and F. Sotiropoulos, Physics of Fluids (1994-present) **24**, 115107 (2012).

[15] M. J. Churchfield, S. Lee, P. J. Moriarty, L. A. Martinez, S. Leonardi, G. Vijayakumar, and J. G. Brasseur, AIAA paper **537**, 2012 (2012).

[16] M. J. Churchfield, S. Lee, J. Michalakes, and P. J. Moriarty, Journal of turbulence p. N14 (2012).

[17] Y.-T. Wu and F. Porté-Agel, Boundary-Layer Meteorology **146**, 181 (2013).

[18] C. L. Archer, S. Mirzaeisefat, and S. Lee, Geophysical Research Letters **40**, 4963 (2013).

[19] R. J. Stevens, D. F. Gayme, and C. Meneveau, Wind Energy **19**, 359 (2016).

[20] N. Hamilton, M. Melius, and R. B. Cal, Wind Energy **18**, 277 (2015).

[21] T. Cebeci, *Analysis of Turbulent Flows with Computer Programs* (Butterworth-Heinemann, 2013).

[22] J. L. Lumley, Atmospheric Turbulence and Radio Wave Propagation pp. 166–178 (1967).

[23] L. Sirovich, Quarterly of Applied Mathematics **45**, 561 (1987).

[24] M. N. Glauser and W. K. George, in *Advances in Turbulence* (Springer, 1987), pp. 357–366.

[25] P. Moin and R. D. Moser, Journal of Fluid Mechanics **200**, 471 (1989).

[26] S. Shah and E. Bou-Zeid, Boundary-Layer Meteorology **153**, 355 (2014).

[27] M. Tutkun, P. V. Johansson, and W. K. George, AIAA **46**, 1118 (2008).

[28] S. Tirunagari, V. Vuorinen, O. Kaario, and M. Larmi, CSI Journal of Computing **1**, 20 (2012).

[29] S. J. Andersen, J. N. Sørensen, and R. Mikkelsen, Journal of Turbulence **14**, 1 (2013).

[30] N. Hamilton, M. Tutkun, and R. B. Cal, Wind Energy **18**, 297 (2015).

[31] D. Bastine, B. Witha, M. Wächter, and J. Peinke, Journal of Physics: Conference Series **524**, 012153 (2014).

[32] C. VerHulst and C. Meneveau, Physics of Fluids **26**, 025113 (2014).

[33] H. S. Kang and C. Meneveau, Measurement Science and Technology **21**, 105206 (2010).